Equivalent circuit representation and analysis of galloping-based wind energy harvesting

Tang, Lihua; Zhao, Liya; Yang, Yaowen; Lefeuvre, Elie

2014

Tang, L., Zhao, L., Yang, Y., & Lefeuvre, E. (2014). Equivalent circuit representation and analysis of galloping-based wind energy harvesting. IEEE/ASME transactions on mechatronics, 1-11.

https://hdl.handle.net/10356/100201

https://doi.org/10.1109/TMECH.2014.2308182

Equivalent Circuit Representation and Analysis of Galloping-Based Wind Energy Harvesting

Lihua Tang, Liya Zhao, Yaowen Yang and Elie Lefeuvre

***Abstract*—Small-scale wind energy can be harvested for wireless sensing applications by exploiting the galloping phenomenon of a bluff body attached to a piezoelectric cantilever. Certain predictive model is required to understand the behavior of such a galloping-based piezoelectric energy harvester (GPEH). Conventional analytical and numerical models have simplified the interface circuit as a pure resistor. In practice, the energy generated by the harvester should be rectified before delivery to a real application. In such a case, the formulation of analytical or numerical model becomes cumbersome considering the complex coupling between the structure, fluid, piezoelectric transducer and practical interface circuit. This paper proposes an equivalent circuit representation approach to predict the performance of GPEHs, capable of incorporating various interface circuits. The mechanical parameters and piezoelectric coupling in the system are represented by standard electronic components and the aerodynamic force by a user-defined component (non-standard). The entire system is modeled in a circuit simulator for system-level simulation and evaluation. The proposed approach is verified by theoretical solution and experiment. Subsequent parametric study is performed to investigate the influence of standard AC and DC interfaces on the GPEH's behavior, with a focus on the threshold of galloping, power output and induced electrical damping.**

***Index Terms*—Wind energy harvesting, equivalent circuit representation, galloping, piezoelectric transducer**

I. Introduction

Wireless sensor networks (WSNs) have been involved in structural health monitoring and environmental monitoring for many years [1]-[3]. Whereas a lot of efforts have been put on energy conservation in WSNs, the limited lifespan of batteries in these systems still hampers their practical deployments. On the other hand, harvesting ambient energy from surrounding environments has been an attractive solution to implement the self-sustained wireless sensor applications in recent years [4]-[6]. Vibration-based energy harvesting has been widely reported in the literature, focusing on the micro-energy conversion from pre-existing structural vibrations into electricity using different methodological techniques [7]-[15]. Wind energy is an alternative energy source pervasively available in the environments. For example, the unmanned aerial vehicles (UAV) experiencing wind gusts can be designed to harvest the gust-induced vibrations for sensing and control purpose in order to maintain the stability [16]. The airflows near the outlets of the heating, ventilation and air conditioning (HVAC) systems in buildings can be recovered to power indoor microclimate control WSNs so as to adapt their outputs to population density, which may save energy on one hand while improving the comfort level of occupants on the other hand.

Aerodynamic instabilities such as vortex-induced vibrations, flutter and galloping have been frequently investigated for effective wind energy conversion. Some studies have investigated the feasibility of harvesting the vortex-induced vibrations of circular cylinders [17]-[20]. The main issue for this technique is that the limited wind speed range for effective power generation requires the matching between the frequency of vortex shedding and the natural frequency of the harvester. For flutter energy harvesting, Kwon [21] experimentally investigated the feasibility of exploiting a T-shaped cantilever to induce flutter oscillations effectively. Li *et al*. [22] developed a bio-inspired piezo-leaf architecture for generating electricity via cross-flow fluttering motions. Other researchers have developed the energy harvesters with flapping wings to convert aeroelastic flutter vibrations into electricity [23]-[26]. Galloping is another aeroelastic instability phenomenon to induce transverse oscillations normal to the wind flow direction where example of this can be seen in the non-circular cross-sectioned bluff bodies that require the wind speed exceeding a critical value. The galloping phenomenon is advantageous to achieve structural vibrations for energy harvesting purpose for its ability of oscillating in infinite wind speed range over vortex-induced vibrations and for its larger amplitude than flutter oscillations [27], [28].

For the first time, Barrero-Gil *et al*. [29] theoretically analyzed the potential use of transverse galloping to harness energy using a single degree-of-freedom (1DOF) model, but no specific energy transduction mechanism was incorporated. Sirohi and Mahadik [30] developed a galloping energy harvester in which a bluff body with equilateral triangular cross-section was attached to two piezoelectric cantilevers, providing a maximum power of 53mW at a wind speed of 4.92m/s. Sirohi and Mahadik [31] proposed another galloping energy harvester using a D-shape bluff body connected in parallel with a piezoelectric cantilever. In these studies,

Lihua Tang was with Nanyang Technological University, Singapore, when preparing this manuscript. He is now a lecturer with Department of Mechanical Engineering at University of Auckland, 20 Symonds Street, 1010 Auckland, New Zealand. (email: l.tang@auckland.ac.nz). Liya Zhao and Yaowen Yang are with Nanyang Technological University, 50 Nanyang Avenue, 639798 Singapore. (e-mail: lyzhao1@e.ntu.edu.sg, cywyang@ntu.edu.sg). Elie Lefeuvre is with the Université Paris-Sud, rue André Ampère, 91405 Orsay Cedex, France (e-mail: elie.lefeuvre@u-psud.fr).

analytical models incorporated with coupled electromechanical behavior have been developed. Following Sirohi and Mahadik, Abdelkefi *et al*. [28] investigated the galloping of square prisms for piezoelectric energy harvesting, with a focus on the influence of the Reynolds number and resistive load on the threshold of galloping and the harvested power level. Abdelkefi *et al*. [32] further studied the influence of geometry of tip bodies on the performance of GPEHs by linear and nonlinear theoretical analyses. Unfortunately, it should be mentioned that the performances of galloping energy harvesters in the aforementioned studies were all evaluated with a pure resistor. WSN nodes or other low-power electronics in practice require a more complex interface circuit for AC-to-DC signal rectification and regulation before the harvested power can be used. As a result, the formulation of analytical or numerical models for system evaluation becomes cumbersome due to the complex coupling in the system: structure, fluid, piezoelectric transducer and practical interface circuit. On the other hand, equivalent circuit models (ECMs) were developed by some researchers for the piezoelectric energy harvesters subjected to base excitations [33]-[35], which could address the modeling challenge for the system with complex interface circuits. Yet, no efforts have been reported on developing the ECM for the GPEHs due to the difficulty in modeling the nonlinear aerodynamic force using standard electronic components.

This paper proposes a modeling approach to evaluate the performance of GPEHs based on equivalent circuit representation, which can tackle various interface circuits and nonlinear aerodynamic forces. The mechanical parameters and piezoelectric coupling in the system are represented by standard linear electronic components and an ideal transformer, respectively. The aerodynamic force is represented by a user-defined electronic component (non-standard) with a nonlinear transfer function. Based on the equivalent circuit representation, the entire GPEH system can be modeled in a circuit simulator for system-level simulation. The proposed approach is first validated by the theoretical solution and experiment. Subsequently, the performances of the GPEH with a standard AC and a standard DC interface circuits are analyzed respectively. Comparison and discussion on the threshold of galloping, power output and electrical damping with different interface circuits are presented followed by a conclusive summary.

II. Mechanism of Galloping

An elastically mounted bluff body (Fig. 1) undergoes galloping normal to the wind flow when the wind speed U exceeds a critical value, providing large-amplitude oscillations. The governing equation of the galloping bluff body can be written as

$$M\ddot{w}(t)+D\dot{w}(t)+Kw(t)=F_Z(t) \tag{1}$$

where M is the mass of the bluff body; D is the damping coefficient; K is the stiffness of the system; $w(t)$ is the displacement of the bluff body along the axis z and $F_Z(t)$ is the aerodynamic force. The overdot denotes the differentiation with respect to time t. $F_Z(t)$ can be expressed as

$$F_Z(t)=\frac{1}{2}\rho_a S U^2 C_{F_Z} \tag{2}$$

where ρ_a is the air density; S is the characteristic area normal to the wind flow and C_{Fz} is the total aerodynamic force coefficient. For a specific cross-section of the bluff body, C_{Fz} is a function of the angle of attack α, and can be determined through experiments [36]. It is common to express C_{Fz} as a polynomial expansion as

$$C_{F_Z}=\sum_{i=1,2,\ldots} A_i(\alpha)^i \tag{3}$$

where A_i (i=1,2,…) are the empirical coefficients for the polynomial fitting [29], [36]. If the bluff body undergoes only translational oscillation without rotation, the angle of attack α can be approximated as

$$\alpha=\frac{\dot{w}(t)}{U} \tag{4}$$

Substituting Eq. (2) into Eq. (1), moving $F_Z(t)$ to the left-hand-side, grouping the mechanical damping term and $F_Z(t)$, and extracting $\dot{w}(t)$, the equation is rearranged as

$$M\ddot{w}(t)+\left\{D-\frac{1}{2}\rho_a SU\left[\sum_{i=1,2,\ldots} A_i\left(\frac{\dot{w}(t)}{U}\right)^{i-1}\right]\right\}\dot{w}(t)+Kw(t)=0 \tag{5}$$

By such, the input aerodynamic force can be considered as an effective nonlinear damping component, making the galloping motions apparently "self-excited". The linear and nonlinear coefficients of the overall damping is then written as

$$D-\frac{1}{2}\rho_a SUA_1 \quad \text{linear} \tag{6a}$$

$$-\frac{1}{2}\rho_a SU\left[\sum_{i=2,3,\ldots} A_i\left(\frac{\dot{w}(t)}{U}\right)^{i-1}\right] \quad \text{nonlinear} \tag{6b}$$

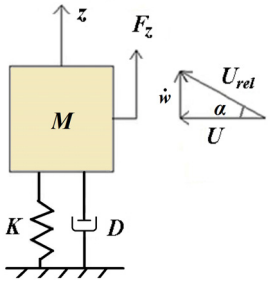

Fig. 1. Schematic of a bluff body undergoing galloping

The criterion for galloping instability is identified as $\partial C_{Fz}/\partial\alpha>0$ by [37], which requires the coefficient A_1 to be positive. Considering the mechanical damping D of the system, the threshold of galloping further requires the overall linear damping (Eq. (6a)) in the system to be negative. This can be explained as follows. For small disturbances, the nonlinear damping component (Eq. (6b)) can be neglected. If the wind speed U is sufficiently low, the linear damping term (Eq. (6a)) is positive and the oscillations due to disturbances will be damped. When U increases and exceeds a critical value $U_{cr}=2D/(A_1\rho_a S)$, the linear damping will become negative, that is, the damping term now contributes positive work to the system and gives rise to the oscillations of the bluff body. With the increase of $\dot{w}(t)$ after the threshold of galloping, the high-order nonlinear damping components in Eq. (6b) will

dominate and make the overall damping back to zero, which ensures the stable limit-cycle oscillations of the system. Hence, the linear damping term determines the threshold of galloping and the nonlinear damping term affects the amplitude of the galloping oscillations. Such "self-excited" and self-limiting characteristic of galloping provides a potential solution for effective wind energy harvesting.

III. Conventional Modeling Method

A practical galloping energy harvester can be implemented by attaching a bluff body on an elastic cantilever beam at its free end and bonding two piezoelectric sheets near its clamped end. The bluff body undergoes galloping when facing an incoming wind flow and develops strain on the beam and piezoelectric sheets, thus generating electrical output fed to the interface circuit, as shown in Fig. 2. Though vortex-shedding may occur in the wake of any bluff body as it results from the instability of the flow profile created by the presence of the body itself, non-circular cross-sectioned bluff bodies are prone to other types of cross-flow-induced instabilities, e.g., galloping [36]. In addition, because of the existence of the cantilever beam that serves as a splitter plate in the wake, regular vortex-shedding is interfered. This further enables such practical GPEH to gallop and suppress vortex-shedding excitation. Hence, throughout the paper, the influence of vortex-shedding on the dynamics of GPEH is neglected. A square-sectioned bluff body is considered in this paper, which has been demonstrated to provide the best performance in laminar flows as compared to other cross sections in preceding experimental study [27].

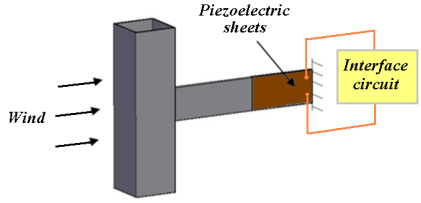

Fig. 2. Schematic of practical GPEH

A simplest way to model the system is to use the 1DOF lumped parameter model [27], [28], [32]. Though distributed parameter models based on Rayleigh-Ritz discretization or exact analytical mode shapes are discussed by Sirohi and Mahadik [31] and Abdelkefi *et al*. [38], they can be finally degraded to the single-mode model as the harvester undergoing galloping oscillates at its fundamental mode. This is consistent with visual observations of beam deformation during galloping in experiment.

Including the piezoelectric coupling and the interface circuit, the governing equations of the lumped parameter model of the GPEH is written as

$$\begin{cases} M\ddot{w}(L_b,t)+D\dot{w}(L_b,t)+Kw(L_b,t)+\theta V(t)=F_Z(t)=\dfrac{1}{2}\rho_a hL_{tip}U^2C_{F_Z} \\ I(t)+C^S\dot{V}(t)-\theta\dot{w}(L_b,t)=0 \end{cases} \quad (7)$$

where L_b is the length of the cantilever beam; $w(L_b,t)$ is the deflection of the beam at the free end (or the translational displacement of the bluff body); M, D and K are the effective mass, damping and stiffness of the system, respectively; θ is the electromechanical coupling coefficient of the system; C^S is the total capacitance of the two piezoelectric transducers which are connected in parallel. It should be mentioned that the hysteresis of the piezoelectric transducers [39] is not considered in this model for simplification. Geometrical parameter h is the edge length of the square section and L_{tip} is the length of the bluff body. Thus, hL_{tip} are the windward area, i.e., the characteristic area of the square-sectioned bluff body. $V(t)$ is the voltage across the piezoelectric transducers and $I(t)$ is the current flow into the interface circuit. Different from the conceptual model of galloping (Fig. 1), the practical galloping energy harvester (Fig. 2) allows the rotation of the bluff body and the attack angle in the expression of C_{Fz} should be modified as

$$\alpha=\frac{\dot{w}(L_b,t)}{U}+w'(L_b,t) \quad (8)$$

where the rotation angle at the free end of the beam can be expressed as

$$w'(L_b,t)=\beta w(L_b,t) \quad (9)$$

where β is the coefficient between the transverse displacement and the rotation angle at the free end of the beam. Now, the galloping is not the purely velocity-dependent damping-controlled instability. The aerodynamics also causes the change of stiffness of the system, resulting in the change of resonant frequency. This will be demonstrated later.

For Eq. (7), analytical solution is cumbersome or even impossible if the interface circuit is complex, e.g., a standard DC interface [40] or more advanced synchronized switching energy harvesting interfaces [41]-[44]. The analytical models for galloping energy harvesters in the literature are all developed by incorporating a pure resistor (standard AC interface circuit). For a pure resistor R_l, substituting $I(t)=V(t)/R_l$ and introducing the variables,

$$\mathbf{X}=\begin{Bmatrix} x_1 \\ x_2 \\ x_3 \end{Bmatrix}=\begin{Bmatrix} w(L_b,t) \\ \dot{w}(L_b,t) \\ V(t) \end{Bmatrix} \quad (10)$$

Eq. (7) can be rearranged in the state space form as

$$\dot{\mathbf{X}}=\begin{Bmatrix} x_2 \\ -\dfrac{D}{M}x_2-\dfrac{K}{M}x_1-\dfrac{\theta}{M}x_3+\dfrac{\rho_a hL_{tip}U^2}{2M}\left[\sum_{i=1,2,\ldots}A_i\left(\dfrac{x_2}{U}+\beta x_1\right)^i\right] \\ \dfrac{\theta}{C^S}x_2-\dfrac{x_3}{R_lC^S} \end{Bmatrix} \quad (11)$$

Using Eq. (11), it is not difficult to obtain the response of the GPEH by employing numerical integration tools, such as ode45 in Matlab.

IV. Equivalent Circuit Representation

In practice, the energy harvesting interface circuits are more complex than a pure resistor (standard AC interface). The output of the harvester should be first rectified to DC signal before delivering the energy to real low-power electronics. To our best knowledge, no solution is available so far in the literature for the evaluation of a GPEH with non-AC interfaces.

To this end, we propose an equivalent circuit modeling method to address this challenging issue. For such a highly coupled aero-electro-mechanical system, we aim at representing the aerodynamic and mechanical parts of the system with equivalent electronic components, such that the overall system can be modeled in electronic simulators for system-level simulation and performance evaluation.

TABLE I
ANALOGIES BETWEEN ELECTRICAL AND MECHANICAL DOMAINS

Equivalent circuit parameters	Mechanical counterparts
Charge: $q(t)$	Displacement: $w(L_b,t)$
Current: $\dot{q}(t)$	Velocity: $\dot{w}(L_b,t)$
Inductance: L	Effective mass: M
Resistance: R	Effective damping: D
Capacitance: C	Reciprocal of effective stiffness: $1/K$
Ideal transformer turn ratio: N	Electromechanical coupling: θ

This approach is extended from the one which has been developed for vibration-based piezoelectric energy harvesters (VPEHs) under base excitations [34], [35], [45]. If we applied the analogies between the electrical and mechanical domains (Table I), Eq. (7) can be rewritten as

$$\begin{cases} L\ddot{q}(t)+R\dot{q}(t)-\frac{1}{2}\rho_a hL_{tip}U^2\left[\sum_{i=1,2,\ldots}A_i\left(\frac{\dot{q}(t)}{U}+\beta q(t)\right)^i\right]+\frac{q(t)}{C}+NV(t)=0 \\ I(t)+C^S\dot{V}(t)-N\dot{q}(t)=0 \end{cases} \tag{12}$$

This is the governing equation of a circuit system shown in Fig. 3. As compared to the equivalent circuit modeling for VPEHs under base excitations, the difficulty for GPEHs lies in the fact that the nonlinear aerodynamic forcing term (Eq. (13)) cannot be represented by an existing or standard electronic component. Fortunately, some circuit simulators such as SIMetrix 6.10i (SIMetrix Technologies Ltd.) allow users to develop arbitrary sources, providing the possibility to implement the circuit representation of the aerodynamic forcing term.

$$-\frac{1}{2}\rho_a hL_{tip}U^2\left[\sum_{i=1,2,\ldots}A_i\left(\frac{\dot{q}(t)}{U}+\beta q(t)\right)^i\right] \tag{13}$$

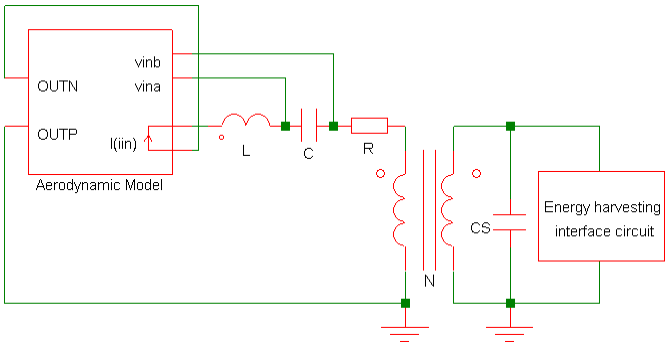

Fig. 3. Equivalent circuit representation of GPEH system

Here onwards, the circuit simulator SIMetrix 6.10i is used for system-level simulation. To define the arbitrary source, its voltage output should be expressed as a function of the variables of current (voltage) through (across) certain electronic components in the circuit (including the arbitrary source itself). Since there is no access to obtain the charge $q(t)$ during simulation, it should be transformed to $V_C(t)$ by the relationship $q(t)=CV_C(t)$, where $V_C(t)$ is the voltage across the capacitor C. Thus, we define the arbitrary source by providing its voltage output expression using two input parameters, $V_C(t)$ and the current through itself $\dot{q}(t)$, as

$$-\frac{1}{2}\rho_a hL_{tip}U^2\left[\sum_{i=1,2,\ldots}A_i\left(\frac{\dot{q}(t)}{U}+\beta CV_C(t)\right)^i\right] \tag{14}$$

In addition, small initial condition for the capacitor C should be applied, which represents the mechanical disturbance to the system. Beyond certain critical wind speed, the galloping will be triggered with this disturbance.

Furthermore, it should be mentioned that although the output signal from the harvester after its threshold of galloping is periodic, AC analysis is not applicable. Transient simulation should be performed to achieve the steady state response of the system (i.e., the output when the harvester oscillates at its limit cycle). For each transient simulation, U is constant and appears in the coefficients of the variables of $V_C(t)$ and $\dot{q}(t)$. In the following analysis of the influence of U on the system behavior, the coefficients of the variables in the user-defined source component will be changed accordingly for different U.

A. Threshold of Galloping from Circuit Perspective

In Section II, we have discussed the threshold of galloping which depends only on the overall linear mechanical damping. When the piezoelectric coupling is introduced (Eq. (7)), the effect of interface circuit on the threshold of galloping is not straightforward and explicit. Fortunately, using the equivalent circuit representation of the entire system, the physical meaning of galloping threshold is clear, that is, the overall linear resistance in the circuit (Fig. 3) becomes negative. For a standard AC interface circuit (a simple resistor R_l), the resistive impedance at the right-hand side of the transformer is

$$\frac{R_l}{1+R_l^2\omega_n^2\left(C^S\right)^2} \tag{15}$$

According to the properties of ideal transformers, the impedance at the right-hand side of the transformer can be moved to the left-hand side by multiplying the square of the turn ratio N. Thus, from the circuit perspective, the threshold of galloping is determined by

$$R-\frac{1}{2}\rho hL_{tip}UA_1+\frac{R_lN^2}{1+R_l^2\omega_n^2\left(C^S\right)^2}\le 0 \tag{16}$$

The critical wind speed can thus be expressed as

$$U_{cr}=\frac{R+\dfrac{R_lN^2}{1+R_l^2\omega_n^2\left(C^S\right)^2}}{\dfrac{1}{2}\rho hL_{tip}A_1} \tag{17}$$

For a complex interface circuit, the critical wind speed for galloping should be determined by circuit simulation.

B. Change of Resonant Frequency from Circuit Perspective

With equivalent circuit representation, the resonant frequency of the system is $(1/L_{total}C_{total})^{1/2}$, where L_{total} and C_{total} are the total inductance and capacitance in the system. Both the

interface circuit and the aerodynamic force will affect C_{total}. When the interface circuit changes from short circuit to open circuit, the impedance at the right-hand side of the transformer in Fig. 3 will change from 0 to pure capacitive C^S, which reduces C_{total} accompanied by the increase of resonant frequency. For the aerodynamic force, we note that the second term $\beta q(t)$ in the round brackets of Eq. (13) is capacitive. Thus, the aerodynamic force affects C_{total} and thus the resonant frequency as well. Unfortunately, because of the nonlinear components in Eq. (13), it is difficult to provide an explicit expression of the resonant frequency of the system but it can be predicted by circuit simulation.

V. Model Validation

To validate the equivalent circuit representation approach, a GPEH prototype is fabricated and tested in the wind tunnel. A simple resistor (standard AC interface) is used so that the theoretical solution of Eq. (11) can also be obtained for comparison with the proposed model based on circuit representation.

The fabricated prototype comprises a bluff body and an aluminum cantilever beam bonded with two piezoelectric transducers, as illustrated in Fig. 4(a). The physical parameters of the piezoelectric cantilever beam are listed in Table II. Two piezoelectric transducers (DuraAct P-876.A12 from Physik Instrumente GmbH & Co. KG.) are connected in parallel with opposite polarity. Thus, the capacitance C^S is 180nF. A square-sectioned bluff body is attached to the free end of the cantilever beam with the parameters listed in Table III. These empirical aerodynamic coefficients are appropriate for laminar flow with high Reynolds number (*Re*) [29]. Given the frontal characteristic dimension of the bluff body of 0.04m, operating wind speed beyond 1.65m/s and kinematic viscosity of 1.5E-5 at the temperature of 20°, *Re* is larger than 4400 and thus these aerodynamic coefficients are safe to be employed.

TABLE II
PARAMETERS OF PIEZOELECTRIC CANTILEVER BEAM

Properties	Substrate	Piezoelectric transducers
Material	Aluminum	DuraAct P-876.A12
Length (mm)	150	61
Width (mm)	30	30
Thickness (mm)	0.6	0.5
Density (kg/m^3)	2700	3825
Capacitance (nF)	---	90

TABLE III
PARAMETERS OF BLUFF BODY

Properties	Value
Cross-section	square
Mass M_{tip} (kg)	0.0268
Length L_{tip} (mm)	150
Section dimensions (mm×mm)	40×40
Empirical aerodynamic coefficients of polynomial expansion of C_{Fz} [29]	A_1=2.3, A_2=0, A_3= -18

TABLE IV
EQUIVALENT CIRCUIT PARAMETERS OF SYSTEM

Item	Value
L (H) / Effective mass M (kg)	0.02816
R (Ω) / Effective damping D (Ns/m)	0.0121
C (F) / Reciprocal of effective stiffness 1/K (m/N)	0.019227
N / Electromechanical coupling: θ (N/V)	0.00037064

Before proceeding to solve Eq. (11) for theoretical solution and conducting circuit simulation, preliminary calculations and vibration tests on a shaker are performed to identify the mechanical parameters of the system.

The effective mass of the harvester is obtained as

$$M=\frac{\int_0^{L_p}\phi^2(x)\left(2\rho_p b_p h_p+\rho_b b_b h_b\right)dx+\int_{L_p}^{L_b}\phi^2(x)\left(\rho_b b_b h_b\right)dx}{\phi^2(L_b)}+M_{tip} \quad (18)$$

where $\phi(x)$ is the first mode shape of the cantilever beam; L_b, b_b, h_b, ρ_b and L_p, b_p, h_p, ρ_p are the length, width, thickness, density of the substrate and piezoelectric sheets, respectively; and M_{tip} is the mass of the bluff body. It should be mentioned that $\phi(x)$ and $\phi'(x)$ thus $\phi(L_b)$ and $\phi'(L_b)$ can be easily determined by finite element analysis [46]. The coefficient β between the transverse displacement and the rotation angle at the free end of the prototyped GPEH is thus determined to be $\beta=\phi'(L_b)/\phi(L_b)$=11.67. The short circuit resonant frequency ω_{nsc} and open circuit resonant frequency ω_{noc} are measured to be 6.84Hz and 6.89Hz from the vibration test, respectively. Thus, the effective stiffness is calculated by $K=\omega_{nsc}^2 M$ and θ is determined by $\theta=\sqrt{\left(\omega_{noc}^2-\omega_{nsc}^2\right)MC^S}$ [27]. The damping ratio ζ is measured using the logarithmic decrement technique and thus damping coefficient D is determined by $D=2\zeta\omega_{nsc}M$. According to the analogies between mechanical and electrical domains (Table I), equivalent circuit parameters in Fig. 3 are also obtained for circuit simulation in SIMetrix. All the identified parameters are listed in Table IV.

During the wind tunnel test, the root of the fabricated prototype is clamped to a metal support (Fig. 4(a)). Wind speed is measured using a hot-wire anemometer. Voltage signal is acquired by NI 9229 DAQ module (National Instruments). The average power is calculated by $P_{ave}=(V_{RMS})^2/R_l$, where V_{RMS} is the Root Mean Square (RMS) voltage across the resistor R_l. The experimental setup for wind tunnel test is shown in Fig. 4(b). Throughout the test, the room temperature is around 20° and the corresponding air density is 1.2041kg/m^3.

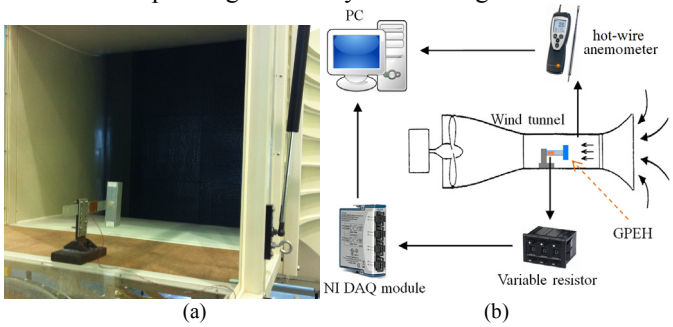

(a) (b)

Fig. 4. (a) Fabricated prototype installed in wind tunnel and (b) experimental setup

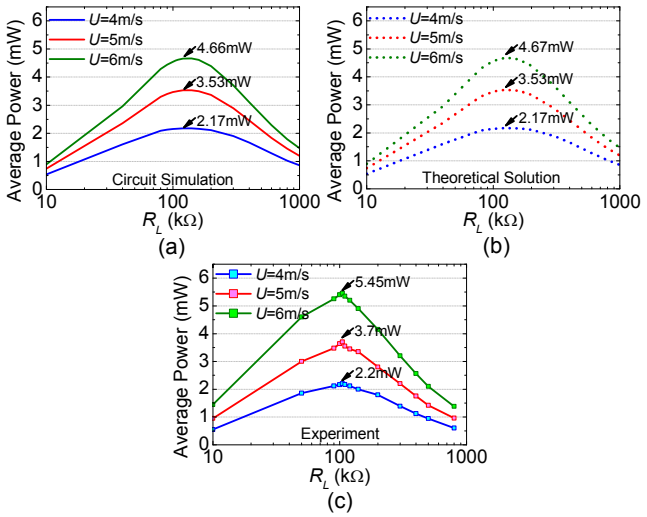

Fig. 5. Comparison of power versus R_l from (a) circuit simulation (b) theoretical solution and (c) experiment

Fig. 5 compares the responses of power versus load from circuit simulation, theoretical solution (Eq. (11)) and experiment. It is indicative to compare the peaks of the power output, which are achieved around 105kΩ~120kΩ for the three wind speeds of 4m/s, 5m/s and 6m/s (In the experiment, more data are collected around the peak to determine the maximum). It is noted that there is very slight difference between the circuit simulation and theoretical solution. As compared to the experimental results, the differences of 1.4%, 4.6% and 14.4% are observed for the three wind speeds, respectively.

We further compare the responses of power versus wind speed and the transient voltage responses at U=4m/s with the optimal load R_l=105kΩ in Fig. 6. The results predicted from the circuit simulation almost overlap the theoretical solution, as shown in Fig. 6(a). As compared to the experimental results, discrepancy becomes significant at the higher wind speed, which is also reflected in Fig. 5. The probable reason for the increased discrepancy is that the aerodynamic force of galloping in the circuit simulation model and the theoretical model is established with the assumption of small angle of attack and the empirical dynamic coefficients of the polynomial function of C_{Fz} (A_1, A_2, …) in Eq. (3) are valid for α up to 16° [36]. At the higher wind speed, the vibration velocity $\dot{w}(L_b,t)$ and the deflection of the cantilever at the tip $w(L_b,t)$ could be very large, making α larger than that limit. In general, the circuit simulation and theoretical model predict very similar trends of responses as experiment for the low wind speed range (<6m/s). It should be emphasized that the discrepancy results from the expression of the aerodynamic force rather than the equivalent circuit representation approach itself. That is why the circuit simulation and theoretical model provide consistent results. Hence, if a more accurate model of aerodynamic force for the higher wind speed can be established, the proposed approach based on equivalent circuit representation for GPEHs is still applicable.

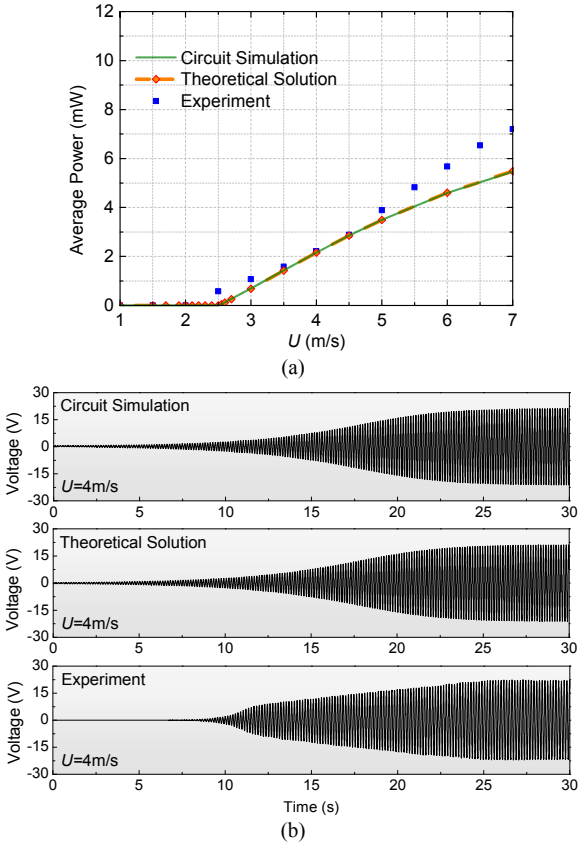

Fig. 6. Comparison of (a) power versus wind speed with R_l=105kΩ and (b) transient voltage responses with R_l=105kΩ from circuit simulation, theoretical solution and experiment

VI. System-Level Simulation and Analysis with Standard AC Interface

With the validated circuit representation model, parametric study is performed to investigate the performance of the GPEH for different interface circuits. We consider a standard AC interface (a pure resistor R_l) first in this section. It should be mentioned that in such a case, theoretical solution for Eq. (7) is available.

Fig. 7 shows the influence of wind speed U and load R_l on the oscillation frequency of the harvester. First, the simulation confirms that oscillation frequency of galloping is consistent with the resonant frequency of the harvester about 6.84Hz (short circuit and no wind flow). The resonant frequency and thus the oscillation frequency are slightly affected by U and R_l. It is noted in Fig. 7(a) that the oscillation frequency declines with the increase of U. This is due to the change of rotation angle at the free end of the cantilever (the second term in the round brackets of Eq. (13), which is capacitive) with different U. In addition, similar to the case of base excitation [34], the oscillation frequency of the GPEH increases from the short-circuit resonant frequency to the open-circuit one with the increase of R_l for a specific wind speed (Fig. 7(b)).

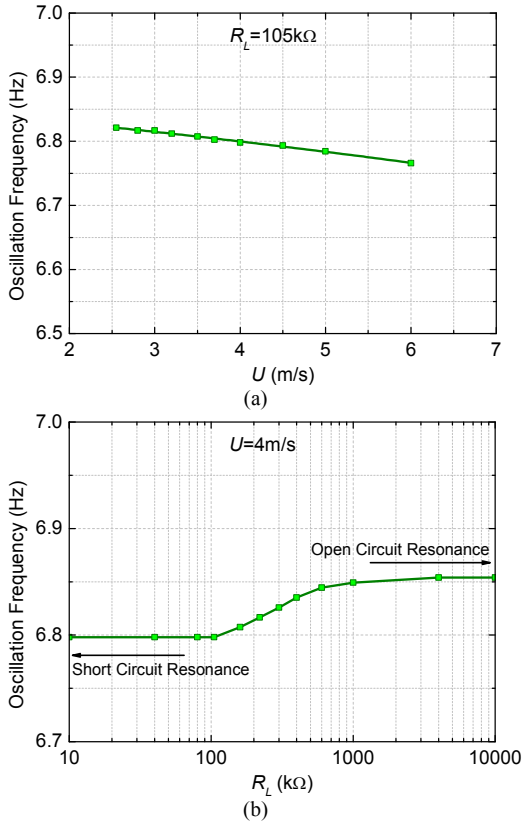

Fig. 7. Influence of (a) U and (b) R_l on oscillation frequency of GPEH

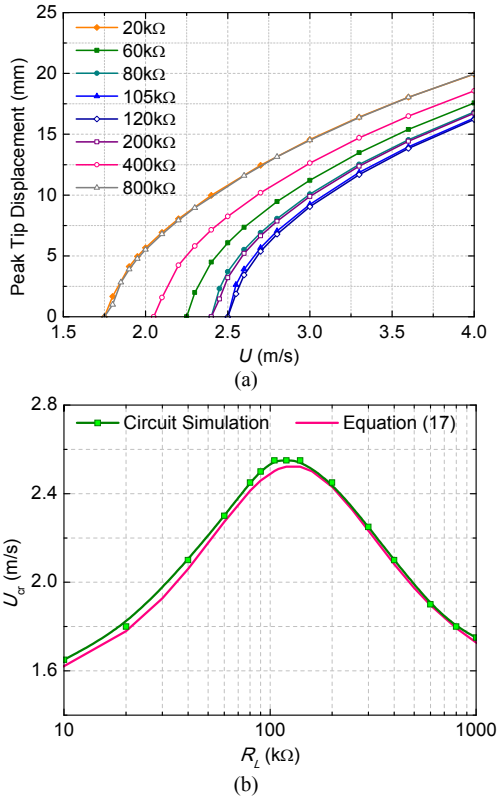

Fig. 8. Threshold of galloping with standard AC interface: (a) response of peak tip displacement and (b) U_{cr} for different R_l

The performance of the GPEH with the standard AC interface is then investigated. Fig. 8 shows the influence of R_l on the threshold of galloping. The response curve of the tip displacement initially moves to the right along the axis of U with R_l increasing up to 120kΩ and then returns with the further increase of R_l, as shown in Fig. 8(a). This corresponds with the variation of the critical wind speed U_{cr} for various R_l, as shown in Fig. 8(b). Galloping is most difficult to occur when R_l reaches around 105kΩ~120kΩ, where U_{cr}=2.52m/s. In addition, it is worth noting that the circuit simulation provides the consistent prediction of U_{cr} as Eq. (17).

Fig. 9 shows the power output of the GPEH for different U and R_l. It is noted in Fig. 9(a) that the growth rate of power (slope of the power response curve) increases with R_l up to 120kΩ. It then declines when R_l further increases. Meanwhile, U_{cr} (the intersect with the horizontal axis) also shifts with R_l. As a result, the optimal power output is achieved around 120kΩ for U>3.5m/s. This can be seen more clearly in Fig. 9(b), in which the power outputs are plot against R_l for five different wind speeds. For U=2m/s, there is no power output for R_l in the range of 40kΩ~400kΩ since this wind speed is less than U_{cr} (Fig. 8(b)) and galloping does not occur. For U=3m/s which is just larger than U_{cr} for 120kΩ, a shallow valley forms at 120kΩ. For U=4m/s, 5m/s and 6m/s, the optimal power is achieved around 120kΩ.

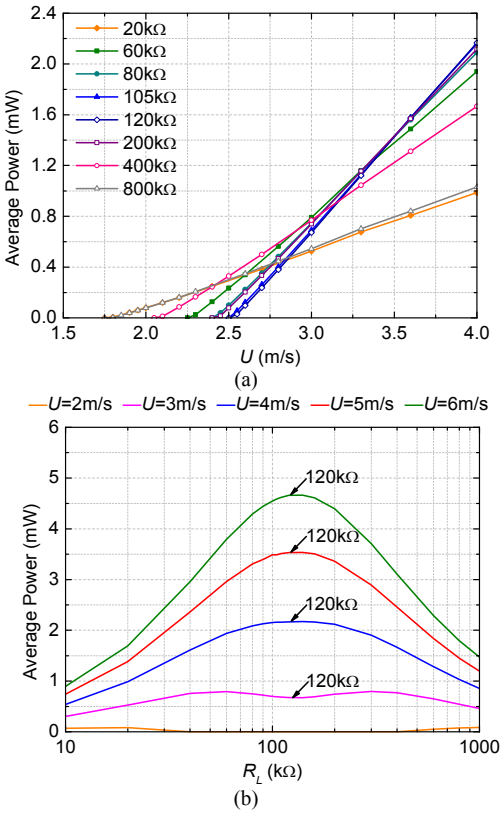

Fig. 9. Power outputs with standard AC interface: (a) power output versus U with different R_l and (b) power output versus R_l at five different U

The electrical damping effect due to the standard AC interface for different U is shown in Fig. 10. For U=2m/s,

galloping does not occur for R_l in the range of 40kΩ~400kΩ. For U=3m/s, 4m/s, 5m/s and 6m/s, galloping occurs for the whole range of R_l and we note that the maximum electrical damping is introduced by R_l≈120kΩ, reflected by the maximum reduction of tip displacement. Interestingly, the maximum damping at R_l=120kΩ is associated with either a valley or a peak in the P_{ave}–R_l response at a specific U, as shown in Fig. 9(b).

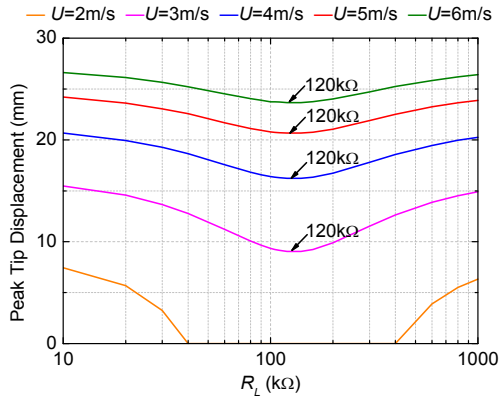

Fig. 10. Electrical damping effect with standard AC interface at five different U

VII. System-Level Simulation and Analysis with Standard DC Interface

In this section, we further investigate the performance of the proposed GPEH with a standard DC interface. To our best knowledge, no analytical or numerical solution is available for such a case. The schematic of the system is shown in Fig. 11, in which the standard DC interface comprises a full-wave rectifier, a filtering capacitor C_{filter} and a load resistor R_l. C_{filter} is properly set to be a large value to ensure a smooth and quasi-constant voltage across R_l when the GPEH is in the steady state.

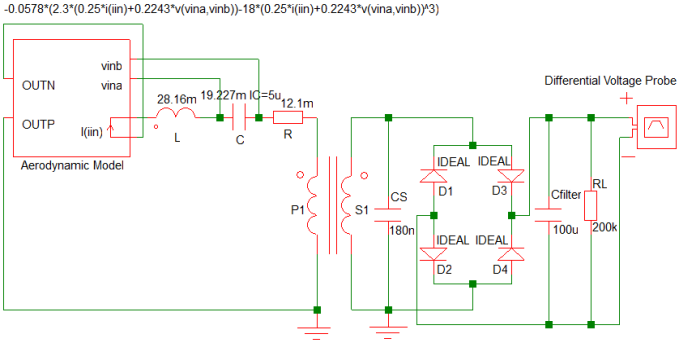

Fig. 11. Schematic of GPEH system with standard DC interface

The responses of tip displacements for different R_l are shown in Fig. 12(a), where the solid lines are obtained with a very small initial disturbance while the dashed lines with a large initial disturbance. If we perform a downward sweep for wind speed, the response will move along the dashed lines. It is noted that for a small R_l (e.g., 20kΩ, 40kΩ), there exist two branches of solution below U=2.25m/s (for the lower branches with small disturbances, galloping does not occur). Single solution is obtained with the increase of R_l values. Fig. 12(b) shows the critical wind speed U_{cr} for galloping with different R_l (small disturbances are considered in simulation). We note that U_{cr} decreases with increasing R_l and when U≥2.25m/s is reached, the occurrence of galloping is ensured regardless of R_l. These observations are quite different from those for the GPEH with a standard AC interface (Fig. 8).

The power responses of the GPEH for different U and R_l are shown in Fig. 13. Except for the small wind speed range where two branches of solution exist, the growth rate of power response (Fig. 13(a)) has a similar trend as that for a standard AC interface (Fig. 9(a)), that is, it first increases with R_l up to 200kΩ and then decreases. As a result, the optimal power output is achieved around 200kΩ for U>2.9m/s. Fig. 13(b) shows this more clearly with the power responses for six different wind speed U. For U=2m/s, there is no power output for R_l<400kΩ since this wind speed is less than U_{cr} (Fig. 12(b)) and galloping does not occur. For U=2.4m/s which is just beyond U_{cr} for 160kΩ (2.15m/s), a valley forms at 160kΩ. For U=3m/s, 4m/s, 5m/s and 6m/s, the optimal power is now achieved around 200kΩ. In addition, it is worth mentioning that the optimal load for the standard DC interface is higher and the corresponding optimal power is smaller than those for the standard AC interface at the same wind speed as compared in Figs. 9 and 13. This is expected as the electrostatic energy from the piezoelectric transducers is being extracted all the time during one period of oscillation for the AC interface while for the standard DC interface, energy extraction stops when the voltage developed on the piezoelectric transducers is lower than the voltage across C_{filter}.

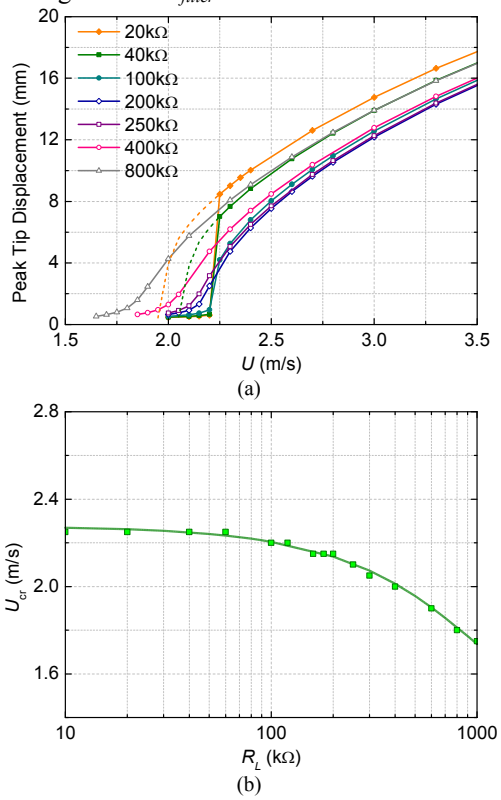

Fig. 12. Threshold of galloping with standard DC interface: (a) response of peak tip displacement and (b) U_{cr} for different R_l

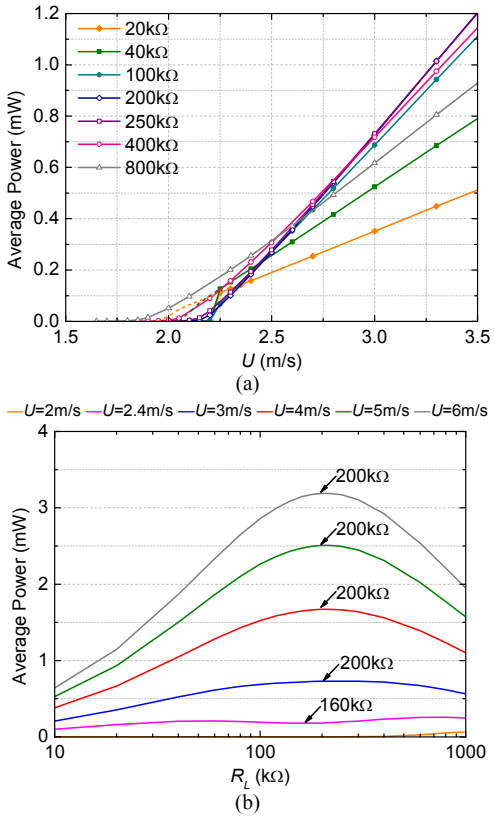

Fig. 13. Power outputs with standard DC interface: (a) power output versus U with different R_l and (b) power output versus R_l at six different U

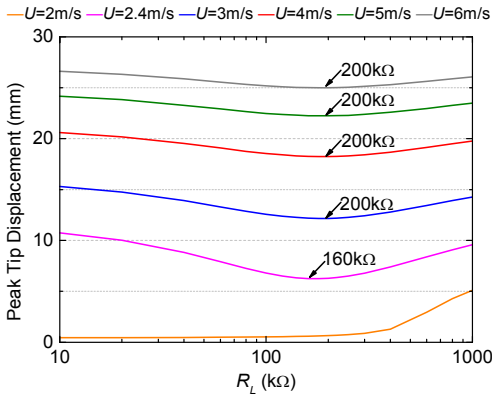

Fig. 14. Electrical damping effect with standard DC interface at six different U

Fig. 14 shows the electrical damping effect due to the DC interface at different wind speed U. For U=2m/s, galloping does not occur for R_l<400kΩ. With the increase of U, galloping occurs for the whole range of R_l. For U=2.4m/s, the maximum electrical damping is introduced at R_l≈160kΩ, corresponding to the valley in the power response (Fig. 13(b)). For U=3m/s, 4m/s, 5m/s and 6m/s, the maximum electrical damping is associated with the optimal power output at R_l≈200kΩ (Fig. 13(b)). In general, the electrical damping introduced by the DC interface is smaller than that by the AC interface as compared in Figs. 10 and 14. For example, at U=4m/s, the tip displacement with the DC interface is damped to a minimum of 18.24mm while that with the AC interface can be damped to a minimum of 16.22mm. This agrees with the smaller optimal power output with the DC interface as compared to the AC interface. In addition, the smaller electrical damping is also associated with the smaller U_{cr} with the DC interface. To be specific, the maximum U_{cr} for the DC interface is 2.25m/s while it is 2.52m/s for the AC interface, as shown in Figs. 12(b) and 8(b).

VIII. Conclusions

This paper has developed an approach to model the GPEH system via equivalent circuit representation. The mechanical parameters and piezoelectric coupling in the system are represented by standard electronic components and the aerodynamic force is modeled by a user-defined (non-standard) electronic component. The ECM of the entire system is then established for system-level simulation and performance evaluation for various interface circuits. The proposed approach based on equivalent circuit representation is verified by the theoretical solution of governing equation and experiment. This equivalent circuit representation approach can be easily extended for the modeling and analysis of other energy harvesting systems with other types of aerodynamic models and with other energy transduction mechanisms, such as electromagnetic or electrostatic transductions.

Parametric study is conducted to investigate the different behaviors of the GPEH with standard AC and DC interface circuits, concentrating on the threshold of galloping, the power output and the induced electrical damping. The main findings based on system-level simulation and analysis can be summarized as follows:

1) *Threshold of Galloping*: The influence of various interface circuits on the threshold of galloping of the GPEH is quite different. For a standard AC interface, U_{cr} for galloping increases first and then drops with R_l. For a standard DC interface, U_{cr} decreases monotonically with R_l. The maximum U_{cr} for AC interface is larger than that for DC interface, in other word, the galloping of GPEH is more difficult to occur with the AC interface.
2) *Power Output*: For both AC and DC interfaces, if the wind speed is large enough (far away from the U_{cr}), optimal power is achieved at a specific R_l. In general, the harvested power with the DC interface is lower than that with the AC interface at a larger optimal load.
3) *Electrical Damping*: For both AC and DC interfaces, the maximum electrical damping corresponds to a valley or a peak in the P_{ave}–R_l response at a specific wind speed U (U>U_{cr}). In general, the DC interface induces smaller electrical damping than the AC interface, associated with its smaller optimal power output and smaller U_{cr} for galloping.

Finally, it should be mentioned that the parametric study is performed with the specific electromechanical coupling of our prototyped GPEH. The influence of the electromechanical coupling on the behavior of a GPEH will be further investigated in the future work.

References

[1] J.P. Lynch and K.J. Loh, "A summary review of wireless sensors and sensor networks for structural health monitoring," *Shock Vib. Digest*, vol.38, no.2, pp.91-130, 2006.

[2] W.Y. Chung and S.J. Oh, "Remote monitoring system with wireless sensors module for room environment," *Sensors and Actuators B: Chemical*, vol.113, no.1,pp.64-70, 2006.

[3] P. Corke, T. Wark, R. Jurdak, W. Hu, P. Valencia, and D. Moore, "Environmental wireless sensor networks," *Proc. IEEE*, vol.98, no.11, pp.1903-1917, 2010.

[4] P. Corke, P. Valencia, P. Sikka, T. Wark, and L. Overs, "Long-duration solar-powered wireless sensor networks," In *ACM Proc.4th Workshop on Embedded Networked Sensors*, pp. 33-37, 2007.

[5] G. Park, T. Rosing, M.D. Todd, C.R. Farrar, and W. Hodgkiss, "Energy harvesting for structural health monitoring sensor networks," *J. Infrastruct. Sys.*, vol.14, no.1, pp.64-79, 2008.

[6] M. Wischke, M. Masur, M. Kröner, and P. Woias, "Vibration harvesting in traffic tunnels to power wireless sensor nodes," *Smart Mater. Struct.*, vol.20, no.8, art. no. 085014, 2011.

[7] E. Halvorsen, E.R. Westby, S. Husa, A. Vogl, N.P. Ostbo, V. Leonov, T. Sterken, and T. Kvisteroy,"An electrostatic energy harvester with electret bias," In *Proc. Int. Conf. Solid-State Sensors, Actuators and Microsystems, 2009. TRANSDUCERS 2009*, pp.1381-1384, 2009.

[8] D.P. Arnold, "Review of microscale magnetic power generation," *IEEE Trans. Magnetics*, vol.43, no.11, pp.3940-3951, 2007.

[9] S.R. Anton and H.A. Sodano, "A review of power harvesting using piezoelectric materials (2003–2006)," *Smart Mater. Struct.*, vol.16, no.3, pp.R1-R21, 2007.

[10] L. Tang, Y. Yang, and C.K. Soh, "Toward broadband vibration-based energy harvesting," *J. Intell. Mater. Sys. Struct.*, vol.21, no.18, pp.1867-1897, 2010.

[11] A.M. Wickenheiser, T. Reissman, W.J. Wu, and E. Garcia, "Modeling the effects of electromechanical coupling on energy storage through piezoelectric energy harvesting," *IEEE/ASME Trans. Mechatronics*, vol.15, no.3, pp.400-411, 2010.

[12] M.F. Lumentut and I.M. Howard, "Electromechanical piezoelectric power harvester frequency response modeling using closed-form boundary value methods," *IEEE/ASME Trans. Mechatronics*, vol.19, no.1, pp.32-44, 2014.

[13] P. Constantinou, P.H. Mellor, and P.D. Wilcox, "A magnetically sprung generator for energy harvesting applications," *IEEE/ASME Trans. Mechatronics*, vol.17, no.3, pp.415-424, 2012.

[14] F. Khameneifar, S. Arzanpour, and M. Moallem, "A piezoelectric energy harvester for rotary motion applications: design and experiments," *IEEE/ASME Trans. Mechatronics*. vol.18, no.5, pp. 1527-1534, 2013.

[15] M.F. Lumentut, L.A. Francis, and I.M. Howard, "Analytical techniques for broadband multielectromechanical piezoelectric bimorph beams with multifrequency power harvesting," *IEEE Trans. Ultrason, Ferroelectr. Freq. Control*, vol.59, no.11, pp.2555-2568, 2012.

[16] Y. Wang and D.J. Inman, "Experimental validation for a multifunctional wing spar with sensing, harvesting, and gust alleviation capabilities," *IEEE/ASME Trans. Mechatronics*, vol.18, no.4, pp.1289-1299, 2013.

[17] H.D. Akaydin, N. Elvin, and Y. Andreopoulos, "Energy harvesting from highly unsteady fluid flows using piezoelectric materials,"*J. Intell. Mater. Sys. Struct.*, vol.21, no.13, pp.1263-1278,2010.

[18] H.D. Akaydin, N. Elvin, and Y. Andreopoulos, "The performance of a self-excited fluidic energy harvester," *Smart Mater. Struct.*, vol.21, no. 2, art. no. 025007, 2012.

[19] V. Sivadas and A.M. Wickenheiser, "A study of several vortex-induced vibration techniques for piezoelectric wind energy harvesting," In *Proc. SPIE Smart Structures and Materials+Nondestructive Evaluation and Health Monitoring*, art. no. 79770F, 2011.

[20] L.A. Weinstein, M.R. Cacan, P.M. So, and P.K. Wright, "Vortex shedding induced energy harvesting from piezoelectric materials in heating, ventilation and air conditioning flows," *Smart Mater. Struct.*, vol.21, no.4, art. no. 045003, 2012.

[21] S.D. Kwon, "A T-shaped piezoelectric cantilever for fluid energy harvesting," *Appl. Phys. Lett.*, vol.97, no.16, art. no. 164102, 2010.

[22] S. Li, J. Yuan, and H. Lipson, "Ambient wind energy harvesting using cross-flow fluttering," *J. Appl. Phys.*, vol.109, no.2, art. no. 026104, 2011.

[23] A. Erturk, W.G.R. Vieira, C. De Marqui, and D.J. Inman, "On the energy harvesting potential of piezoaeroelastic systems," *Appl. Phys. Lett.*, vol.96, no.18, art. no. 184103, 2010.

[24] M. Bryant and E. Garcia, "Modeling and testing of a novel aeroelastic flutter energy harvester," *J. Vib. Acoust.*, vol.133, no.1, art. no. 011010, 2011.

[25] V.C. Sousa, M. de M Anicézio, C. De Marqui, and A. Erturk, "Enhanced aeroelastic energy harvesting by exploiting combined nonlinearities: theory and experiment," *Smart Mater. Struct.*, vol.20, no.9, art. no. 094007, 2011.

[26] C. Boragno, R. Festa, and A. Mazzino, "Elastically bounded flapping wing for energy harvesting," *Appl. Phys. Lett.*, vol.100, no.25, art. no.253906, 2012.

[27] Y. Yang, L. Zhao, and L. Tang,"Comparative study of tip cross-sections for efficient galloping energy harvesting," *Appl. Phys. Lett.*, vol.102, no.6, art. no. 064105, 2013.

[28] A. Abdelkefi, M.R. Hajj, and A.H. Nayfeh, "Power harvesting from transverse galloping of square cylinder," *Nonlinear Dynamics*, vol.70, No.2, pp.1355-1363, 2012.

[29] A. Barrero-Gil, G. Alonso, and A. Sanz-Andres, "Energy harvesting from transverse galloping," *J. Sound Vib.*, vol.329, no.14, pp.2873-2883, 2010.

[30] J. Sirohi and R. Mahadik, "Piezoelectric wind energy harvester for low-power sensors,"*J. Intell. Mater. Sys. Struct.*, vol.22, no.18, pp.2215-2228, 2011.

[31] J. Sirohi and R. Mahadik, "Harvesting wind energy using a galloping piezoelectric beam," *J. Vib. Acoust.*, vol.134, no.1, art. no. 011009, 2012.

[32] A. Abdelkefi, M.R. Hajj, and A.H. Nayfeh, "Piezoelectric energy harvesting from transverse galloping of bluff bodies," *Smart Mater. Struct.*, vol.22, no.1, art. no. 015014, 2013.

[33] N.G. Elvin and A.A. Elvin, "A general equivalent circuit model for piezoelectric generators," *J. Intell. Mater. Sys. Struct.*, vol.20, no.1, pp.3-9, 2009.

[34] Y. Yang and L. Tang, "Equivalent circuit modeling of piezoelectric energy harvesters," *J. Intell. Mater. Sys. Struct.,* vol.20, no.18, pp.2223-2235, 2009.

[35] L. Tang and Y. Yang, "A multiple-degree-of-freedom piezoelectric energy harvesting model," *J. Intell. Mater. Sys. Struct.*,vol.23, no.14, pp.1631-1647, 2012.

[36] M.P. Païdoussis, S.J. Price, and E. De Langre, *Fluid-structure Interactions: Cross-flow-induced Instabilities*, Cambridge University Press, 2010.

[37] J.P. Den Hartog, *Mechanical Vibrations*, McGraw-Hill, 1956.

[38] A. Abdelkefi, Z. Yan, and M.R. Hajj, "Modeling and nonlinear analysis of piezoelectric energy harvesting from transverse galloping," *Smart Mater. Struct.*, vol.22, no.2, art. no. 025016, 2013.

[39] Y.L.Zhang, M.L.Han, M.Y.Yu, C.Y.Shee, and W.T.Ang, "Automatic hysteresis modeling of piezoelectric micromanipulator in vision-guided micromanipulation systems," *IEEE/ASME Trans. Mechatronics*, vol.17, no.3, pp.547-553, 2012.

[40] Y.C. Shu and I.C. Lien, "Analysis of power output for piezoelectric energy harvesting systems," *Smart Mater. Struct.*, vol.15, no.6, pp.1499-1512, 2006.

[41] E. Lefeuvre, A. Badel, C. Richard, and D. Guyomar, "Piezoelectric energy harvesting device optimization by synchronous electric charge extraction," *J. Intell. Mater. Sys. Struct.*, vol.16, no.10, pp.865-876, 2005.

[42] I.C. Lien, Y.C. Shu, W.J. Wu, S.M. Shiu, and H.C. Lin, "Revisit of series-SSHI with comparisons to other interfacing circuits in piezoelectric energy harvesting," *Smart Mater. Struct.*, vol.19, no.12, art. no. 125009, 2010.

[43] L. Tang and Y. Yang, "Analysis of synchronized charge extraction for piezoelectric energy harvesting," *Smart Mater. Struct.*, vol.20, no.8, art. no. 085022, 2011.

[44] J. Liang and W.H. Liao, "Improved design and analysis of self-powered synchronized switch interface circuit for piezoelectric energy harvesting systems," *IEEE Trans. Industrial Electronics*, vol.59, no.4, pp.1950-1960, 2012.

[45] J. Liang and W.H. Liao, "Impedance modeling and analysis for piezoelectric energy harvesting systems," *IEEE/ASME Trans. Mechatronics*, vol.17, no.6, pp.1145-1157, 2012.

[46] L. Zhao, L. Tang, and Y. Yang, "Comparison of modeling methods and parametric study for a piezoelectric wind energy harvester," *Smart Mater. Struct.*, vol.22, no.12, art. no.125003, 2013.